Proceedings of The Magnetized Plasma in Galaxy Evolution
Sep. 27th – Oct. 1st 2004, Jagiellonian University, Kraków, Poland
Eds. K.T. Chyży, K. Otmianowska-Mazur, M. Soida and R.-J. Dettmar

Role of Magnetic Field in Star Formation Process

Kohji Tomisaka[1], M. N. Machida[2], T. Matsumoto[3], and T. Hanawa[2]

[1]National Astronomical Observatory, Mitaka, Tokyo 181-8588, Japan
[2]Center for Frontier Science, Chiba University, Inageku, Chiba 263-8522, Japan
[3]Faculty of Humanity and Environment, Hosei University, Chiyoda-ku, Tokyo 102-8160, Japan

Abstract

Three-dimensional MHD nested grid simulations on the magnetized cloud collapse are presented. It is shown that the fragmentation process is much affected by the magnetic field as well as the rotation motion in the aligned rotator of $\mathbf{B} \parallel \mathbf{\Omega}$. Magnetic field suppresses the fragmentation of the first core. For the cloud of $\mathbf{B} \nparallel \mathbf{\Omega}$ (non-aligned rotator), the angular momentum is efficiently transferred by the magnetic field and the alignment is achieved by the first core formation epoch.

1 Fragmentation and Binary Formation

Since binary stars are much popular than single stars, to understand star formation we have to understand binary formation. An isothermal cloud with the thermal-to-gravitational energy ratio $\alpha \simeq 0.5$ experiences the run-away collapse, in which the central density increases greatly in a finite time. Finally a hydrostatic core forms in the cloud (Larson 1969). Fragmentation in this first core is a candidate to explain the binary formation (Matsumoto & Hanawa 2003; Machida et al. 2004a). Since a thinner disk tends to fragment more easily, the rotation and the magnetic field (B-field) seem to encourage the fragmentation. On the contrary, B-field has an effect to remove the angular momentum (magnetic braking) and may discourage the fragmentation. First, we try to explore the effect of the B-field on the fragmentation process (see Machida et al. 2004a, b, and c).

In the isothermal collapse and the subsequent adiabatic core formation, the density increases from that of the molecular cloud $n \sim 10^2 - 10^3\mathrm{cm}^{-3}$ to that of the first core $n \sim 10^{11}\mathrm{cm}^{-3}$. This requires a large dynamic range in density. Finite-difference schemes with uniform grid spacing fail to represent such density distributions and cannot trace the evolution. We employ the nested grid technique, in which a number of grid systems with different spacings are prepared and a finer grid covers the central high-density part while a coarser one is used to represent the global structure (Tomisaka 1996). We consider a cylindrical cloud in a hydrostatic balance between the self-gravity and the repulsive forces (thermal and magnetic pressure force and centrifugal force; for more detailed model setting, see Machida et al. 2004a). When the magnetic to thermal pressure ratio is uniform irrespective of the radius r, the density, the rotation velocity, and the magnetic flux density are given as

$$\rho_0(r) = \rho_c \left[1 + (r^2/8H^2)\right]^{-2},$$

$$v_{\phi 0}(r) = r\Omega_c \left[1 + (r^2/8H^2)\right]^{-1/2},$$

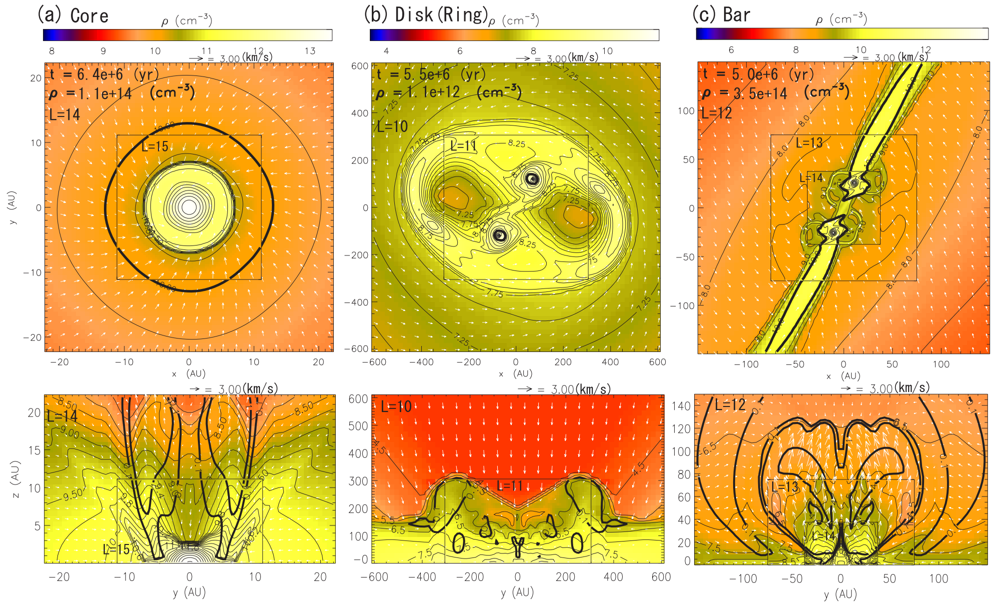

Figure 1: Three typical models: models A (left), B (center), and C (right). The upper and lower panels represent a pole-on and edge-on views, respectively.

and

$$B_{z0}(r) = B_c \left[1 + (r^2/8H^2)\right]^{-1},$$

where H represents the scale-height as

$$H = \left[(c_s^2 + B_c^2/8\pi\rho_c)/(4\pi G\rho_c - 2\Omega_c^2)\right]^{1/2}.$$

We add perturbations to this equilibrium and start dynamical contraction. After choosing the amplitude of the axisymmetric perturbation $\delta\rho/\rho_0 = 0.1$, we have two parameters to specify the balance: normalized rotation speed $\omega \equiv \Omega_c/(4\pi G\rho_c)^{1/2}$ and normalized magnetic pressure $\alpha \equiv B_c^2/4\pi\rho_c c_s^2$ and another parameter to specify the amplitude of the non-axisymmetric perturbation A_{m2}.

2 Fragmentation

Figure 1 indicates typical structure of the first core. Model A ($\omega = 0.1$, $\alpha = 1$, and $A_{m2} = 0.01$) shows no fragmentation and leaves an unfragmented core. Strong B-field and small $m = 2$ amplitude induce no fragmentation. While models B ($\omega = 0.5$, $\alpha = 0.01$, and $A_{m2} = 0.01$) and C ($\omega = 0.5$, $\alpha = 1$, and $A_{m2} = 0.2$) indicate fragmentation. This shows there are two types of fragmentation: a ring or a spiral forms first and two high-density cores appear in it (model B: disk or ring fragmentation) and a bar is formed and in the bar two high-density cores form which continue to contract (bar fragmentation). Since the orbital angular momenta of the cores in the bar fragmentation models are small and the orbits are

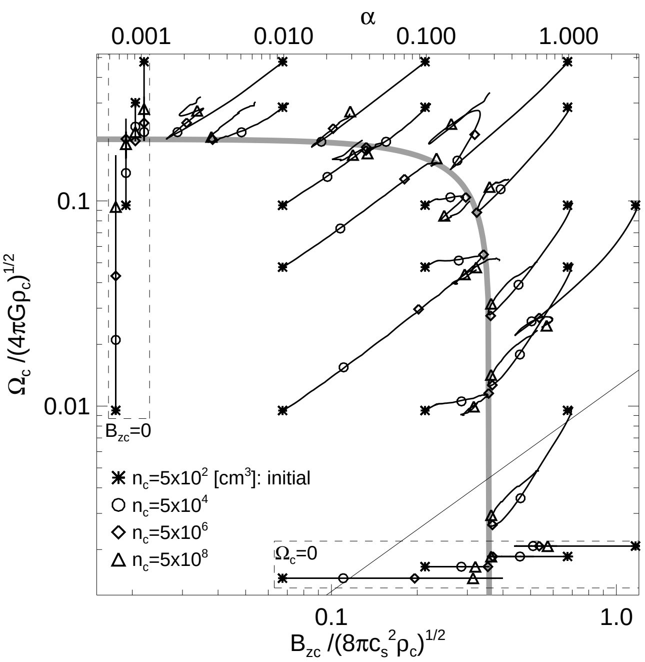

Figure 2: The evolution of normalized B-field strength and the normalized angular rotation speed. The cloud evolves in the sequence of asterisk, circle, square and triangle.

extremely elongated, such cores tend to collide each other and form a single core spinning rapidly.

3 Spin-Magnetic Field Relation

In Figure 2, we plot the time evolution of the normalized B-field strength and the normalized angular rotation speed (x-axis: $B_{z,c}/[8\pi\rho_c c_s^2]^{1/2}$ and y-axis: $\Omega_c/[4\pi G\rho_c]^{1/2}$). This figure indicates clearly there are two types of evolutions, that is, those moving from the upper-right to the lower-left and those moving oppositely. We can see the evolutionary paths converge to a curve indicated with a thick line, which is well expressed as

$$\frac{\Omega_c^2}{(0.2)^2\ 4\pi G\rho_c} + \frac{B_{\rm zc}^2}{(0.36)^2\ 8\pi c_s^2\rho_c} = 1.$$

Since the rotation motion and B-field strength are large enough above the line, a disk is promptly formed in this support-excess region. In this case, B_c and Ω_c are kept constant while ρ_c increases with time. Thus the point moves to the lower-left direction. After a disk is formed, the magnetic frozen-in and angular momentum conservation demand that both B_c and Ω_c are proportional to the column density $\propto \sigma_c$. Since $\sigma \propto \rho^{1/2}$ in the thin self-gravitating disk, both normalized B_c and Ω_c show slight evolutions as long as the disk continues to contract radially (in the cylindrical coordinate).

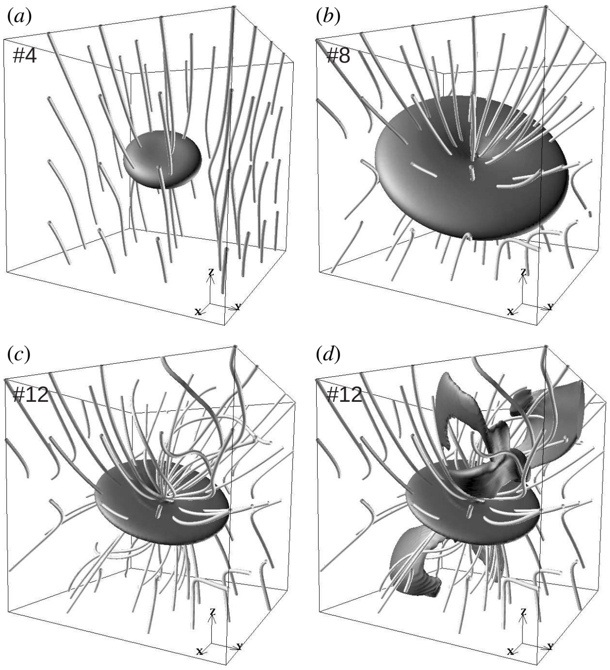

Figure 3: Three dimensional structures of density and B-field in the final stage. The box sizes are (a) 0.356 pc, (b) 4590 AU, and (c and d) 287 AU, where (d) shows the positive radial velocity (outflows) as $v_r = 10c_s$ isovelocity surfaces.

While, gas contracts spherically radially in the support-deficient region below the line. Spherically radial contraction demands that B_c and Ω_c are proportional to $\rho_c^{2/3}$. This leads both normalized B_c and Ω_c to increase with time proportional to $\rho_c^{1/6}$, which indicates the evolution toward the upper-right direction. If we consider the magnetic braking, $\Omega_c/\rho_c^{2/3}$ decreases with time but $B_c/\rho_c^{2/3}$ keeps constant. Thus, the magnetic braking increases the ratio of normalized B_c to that of Ω_c. The nearly horizontal paths near the vertical part of the convergence represent the evolution driven by the efficient magnetic braking.

After reaching the curve, the central part of the cloud forms a disk (or a bar). The centrifugal force is dominant to form a disk on the horizontal part of the curve while the magnetic support is important on the vertical part of the curve. Numerical simulations show us that all the fragmentation models have sufficiently fast rotation speed as $\Omega_c \gtrsim 0.2(4\pi G\rho_c)^{1/2}$ at the first core formation epoch. This seems to indicate that clouds which reach the horizontal part of the curve (a centrifugal force dominated disk) are unstable for fragmentation. Those captured by the vertical part of the curve (a magnetically dominated disk) are stable and continue to be non-fragmentation cores. Since the cloud evolves as $B_c \propto \Omega_c$, the cloud with

$$\frac{\Omega_0}{B_0} \gtrsim \frac{G^{1/2}}{2^{1/2}c_s} \sim 3 \times 10^{-7}\mathrm{yr}^{-1}\mu\mathrm{G}^{-1}$$

will fragment after the core formation. Starless core L1544 has $B_0 \simeq 11 \pm 2\mu$G (Crutcher & Troland 2000) and $\Omega_0 \simeq (1.3 - 4.2) \times 10^{-6}\mathrm{yr}^{-1}$ (Ohashi et al. 1996, Williams et al. 1999),

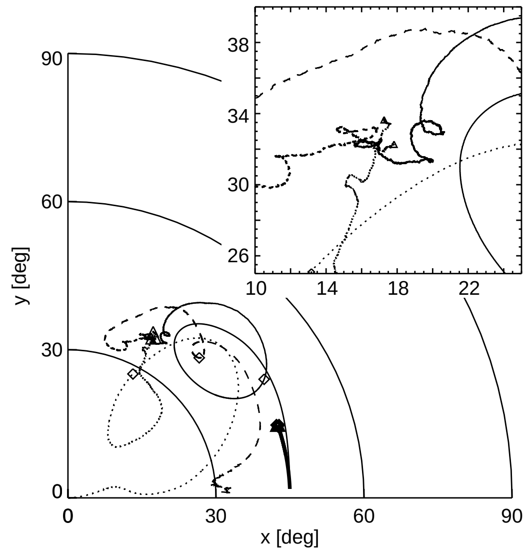

Figure 4: Loci of directions of the central magnetic field $\mathbf{B}_c$ (thin solid line), the central angular momentum $\mathbf{J}_c$ (dotted line), the normal vector of the disklike density structure $\mathbf{n}$ (dashed line), and the magnetic field at the boundary $\mathbf{B}_b$ (thick line). Diamonds denote the stage of adiabatic core formation, and triangles denote the final stage. Inset: Detail of the convergence point.

which gives a marginal Ω-to-B ratio as $\Omega_0/B_0 \sim (1.2-3.8)\times 10^{-7}\mathrm{yr}^{-1}\mu\mathrm{G}^{-1}$. Since the critical rotation speed for fragmentation increases with the magnetic strength, *the B-field suppresses the fragmentation.*

4 Non-Aligned Rotator

We have examined the evolution of aligned rotator in which the angular momentum vector and B-field vector are parallel each other. In this section, we examine whether this assumption is valid or not. As for the alignment of outflow and B-field, B-field near the protostars like IRAS 16293-2422 and L1551 IRS5 observed by the 1mm radio observation is parallel to the outflow direction (Tamura et al. 1995). Larger-scale B-fields observed in Bok globules (Wolf et al. 2003) sometimes indicate poor alignment with the outflow. To explore the alignment of B-field, angular momentum $\mathbf{J}$, and the disk normal $\mathbf{n}$, 3D MHD simulations have been done for non-aligned rotator $\mathbf{J} \nparallel \mathbf{B}$ (see Matsumoto & Tomisaka 2004).

We assume a spherical cloud 1.68 times more massive than the critical Bonnor-Ebert isothermal cloud with the central density of $\rho_c = 10^{-19}\mathrm{g\,cm}^{-3}$. This cloud is uniformly rotating with $7.11\times 10^{-7}\mathrm{yr}^{-1}$ and is immersed in a uniform B-field of 18.6μG. This setup gives $\alpha \equiv E_{\rm th}/|E_{\rm grav}| = 0.5$, $\beta \equiv E_{\rm rot}/|E_{\rm grav}| = 0.02$, and $\gamma \equiv E_{\rm mag}/|E_{\rm grav}| = 0.72$. Although γ seems large, this cloud is magnetically supercritical, since the critical B-flux $B_{\rm cr} \equiv G^{1/2}\sigma/2\pi$ is equal to 74.5μG for this cloud.

Figure 3 shows the snapshots of the contracting disk when the outflow is ejected owing to the magneto-centrifugal wind mechanism seen in (d). The z-axis is taken parallel to the initial **J**. From large (a) to small (c) scales, we can see the direction of disk normal changes. This directional change coincides with the rotation direction (counter-clockwise viewing from the z-axis). This comes from the fact that central rotation speed Ω_c increases as $\propto \rho_c^{1/2}$. Although the direction of disk normal **n** changes, it always parallel to the local **B**, which means the direction of local **B** rotates counter-clockwise from large scale to small scale.

Figure 4 shows the time evolution of directions of three vectors (**B**, **J**, and **n** at the center) are initially separated at 45° but they converge with each other as the cloud contracts. Although the large-scale **J**, which points toward the z-axis, and the large-scale **B** has an angle of 45°, these three small-scale vectors coincide within a degree. This indicates that the component of **J** perpendicular to **B** is effectively transferred by magnetic braking and that the disk is formed perpendicular the small-scale **J** and **B**. It is concluded that the analysis for the fragmentation condition in the magnetized aligned cloud $\mathbf{J} \parallel \mathbf{B}$ is applicable to the non-aligned cloud $\mathbf{B} \nparallel \mathbf{J}$.

Acknowledgments

This research was supported in part by the Ministry of Education, Science, Sports and Culture, Grants-in-Aid for Scientific Research (C) 14540233 (K.T.), for Young Scientists (B) 14740134 and 16740115 (T.M.), and for Scientific Research (B) 13011204 (T.H.). Numerical computations were carried out on VPP5000 at the Astronomical Data Analysis Center, ADAC, of the National Astronomical Observatory of Japan.

References

Crutcher R.M., Troland T.H., 2000, ApJ, 537, L139

Larson R. B., 1969, MNRAS, 145, 271

Machida M.N,. Tomisaka K., Matsumoto T., 2004a, MNRAS, 348, L1

Machida M.N., Matsumoto T., Tomisaka K., Hanawa T., 2004b, submitted to MNRAS

Machida M.N., Matsumoto T., Hanawa T., Tomisaka K., 2004c, submitted to MNRAS

Matsumoto T., Hanawa T., 2003, ApJ, 595, 913

Matsumoto T., Tomisaka K., 2004, ApJ, 616, 266

Ohashi N., Hayashi M., Ho P.T.P, Momose M., Hirano N., 1996 ApJ, 466, 957

Tamura M., Hough J.H., Hayashi S.S., 1995, ApJ, 448, 346

Tomisaka K., 1996, PASJ, 48, 701

Williams J.P., Myers P.C., Wilner D.J., Francesco J.D., 1999, ApJ, 513, L61

Wolf S., Launhardt R., Henning T., 2003, ApJ, 592, 233